IOP Publishing | International Atomic Energy Agency Nuclear Fusion

Nucl. Fusion **58** (2018) 056018 (17pp) https://doi.org/10.1088/1741-4326/aab2c8

Edge transport and mode structure of a QCM-like fluctuation driven by the Shoelace antenna

T. Golfinopoulos[a], B. LaBombard, D. Brunner, J.L. Terry, S.G. Baek, P. Ennever, E. Edlund, W. Han, W.M. Burke, S.M. Wolfe, J.H. Irby, J.W. Hughes, E.W. Fitzgerald, R.S. Granetz, M.J. Greenwald, R. Leccacorvi, E.S. Marmar, S.Z. Pierson, M. Porkolab, R.F. Vieira, S.J. Wukitch and The Alcator C-Mod Team

Plasma Science and Fusion Center, Massachusetts Institute of Technology, Cambridge, MA 02139, United States of America

E-mail: golfit@mit.edu

Received 30 November 2017, revised 31 January 2018
Accepted for publication 28 February 2018
Published 21 March 2018

Abstract

The Shoelace antenna was built to drive edge fluctuations in the Alcator C-Mod tokamak, matching the wavenumber ($k_\perp \approx 1.5$ cm^{-1}) and frequency ($30 \lesssim f \lesssim 200$ kHz) of the quasi-coherent mode (QCM), which is responsible for regulating transport across the plasma boundary in the steady-state, ELM-free Enhanced D_α (EDA) H-mode. Initial experiments in 2012 demonstrated that the antenna drove a resonant response in the edge plasma in steady-state EDA and transient, non-ELMy H-modes, but transport measurements were unavailable. In 2016, the Shoelace antenna was relocated to enable direct measurements of driven transport by a reciprocating Mirror Langmuir Probe, while also making available gas puff imaging and reflectometer data to provide additional radial localization of the driven fluctuation. This new data suggests a ~4 mm-wide mode layer centered on or just outside the separatrix. Fluctuations coherent with the antenna produced a radial electron flux with $\Gamma_e/n_e \sim 4$ m s^{-1} in EDA H-mode, smaller than but comparable to the QCM level. But in transient ELM-free H-mode, Γ_e/n_e was an order of magnitude smaller, and driven fluctuations reduced by a factor of $\gtrsim$3. The driven mode is quantitatively similar to the intrinsic QCM across measured spectral quantities, except that it is more coherent and weaker. This work informs the prospect of achieving control of edge transport by direct coupling to edge modes, as well as the use of such active coupling for diagnostic purposes.

Keywords: fusion, tokamak, shoelace antenna, edge transport, edge fluctuations, Alcator C-Mod, quasi-coherent mode

(Some figures may appear in colour only in the online journal)

1. Introduction

The practical realization of fusion energy within the tokamak framework depends, in part, upon the identification of viable steady-state, reactor-relevant, high-performance operational regimes. A common feature between such regimes is the presence of a benign, continuous fluctuation in the plasma edge [1].

Examples of such continuous fluctuations include the weakly coherent mode (WCM) associated with the I-mode regime [2, 3], the Edge harmonic oscillation of the quiescent H-mode [4, 5], the Low- and high-frequency quasi-coherent modes of the high recycling steady regime [6, 7], and the quasi-coherent mode (QCM) of the enhanced D_α (EDA) H-mode [8–14]. These fluctuations sustain high-performance regimes by making the edge permeable to impurities without significantly degrading energy confinement. While edge localized

[a] Author to whom any correspondence should be addressed.

modes (ELMs) can also fulfill this role in modestly-sized tokamaks, their violent, bursting nature does not extrapolate to a reactor-scale device, according to current understanding, as it would deliver unacceptably-high transient heat loads to the divertor [15–17]. Confinement regimes bearing one of the continuous edge fluctuations mentioned above avoid this problem, delivering a steady heat flow to the divertor without ELMs, and are therefore more attractive for a reactor scenario.

In order to study the exploitation of continuous edge modes for the purpose of controlling edge transport, and to inform the development of actuators to produce such modes, a novel 'Shoelace' antenna was installed on the Alcator C-Mod tokamak [18, 19]. It was designed to inductively excite an edge fluctuation at the QCM wave number and frequency. Initial operation showed that the antenna-driven mode was aligned with and guided by the background field, resonant at the QCM frequency, and of comparable, though smaller, amplitude to the intrinsic fluctuation [20–22]. However, direct measurements of driven flows were unavailable because appropriate diagnostics—in particular, the mirror Langmuir probe (MLP, [14, 23])—only marginally mapped to the antenna along field lines on the last closed flux surface (LCFS), a necessary condition for measuring the driven density fluctuation due to the field-line-guided nature of the coupled mode.

In 2016, the antenna was moved toroidally to sit alongside a suite of diagnostics—including the MLP, gas puff imaging (GPI), and reflectometry—giving the first robust, direct characterization of driven particle and thermal flows, as well as the driven mode's radial structure. The power available to the antenna was quadrupled, doubling the amplitude of the vacuum-field perturbation, improving signal robustness, and probing linearity in plasma response over a wider power window.

The discussion of these new measurements is organized as follows: section 2 describes changes to the original Shoelace antenna configuration. Results are presented in section 3, focusing on driven edge flows, as well as radial mode localization, with the appendix detailing data analysis techniques. These results are then placed in the context of developing actuators for control of impurity exhaust by active stimulation of continuous edge fluctuations in section 4. The discussion concludes in section 5.

2. Experimental setup

2.1. Antenna

The construction and operation of the Shoelace antenna has been described elsewhere [20–22]; however, a brief overview is provided here. A single strand of molybdenum wire is wound back and forth on a set of spring-loaded posts to create 19 rungs, with electrical current running in opposing directions in adjacent rungs. The winding reaches the top of the antenna and folds back upon itself, so that the inner 17 rungs have two layers, each—the 'shoelace' name is meant to suggest this winding pattern. The spacing between the rungs recreates the perpendicular wave number, $k_\perp \approx 1.5$ cm^{-1}, of the QCM, as well as the WCM [3, 24–26]. The winding is inclined at an 11° angle to align with the edge background field at $q_{95} \sim 4$. In the original antenna configuration, the winding angle was ∼13° to align with the equilibrium field at $q_{95} \sim 3$.

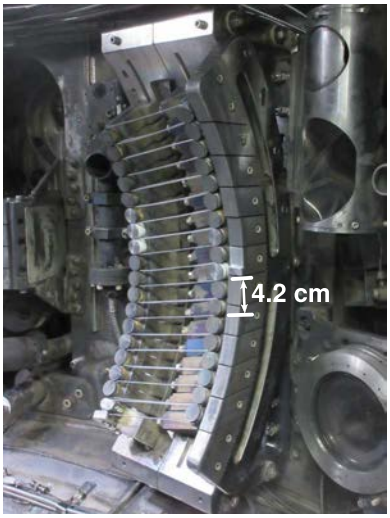

Figure 1. The Shoelace antenna mounted inside the Alcator C-Mod vacuum vessel, as configured in its shifted location for operation in the 2016 experimental campaign.

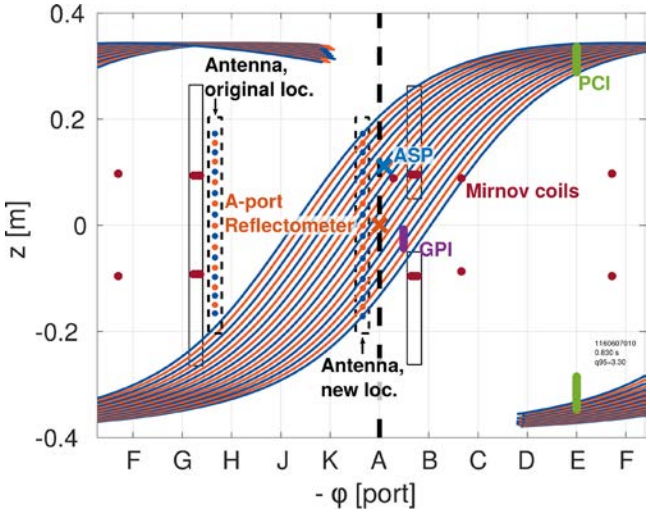

Figure 2. Field lines along the LCFS that map to antenna rungs (with $q_{95} \approx 3.3$), together with locations of fluctuation diagnostics, and old and new antenna positions.

Figure 1 shows the antenna mounted in its new location, translated 107.5° clockwise toroidally from its original location, while figure 2 shows how the new antenna rung locations, projected radially onto the LCFS, map to fluctuation diagnostics. In the original antenna location, the mapped field lines were well-covered by the phase contrast imaging (PCI), Mirnov coil, and polarimeter diagnostics, which allowed good characterization of the driven mode's perpendicular wave number and resonant characteristics. However, only the lowest antenna rungs mapped to the the MLP, and only at $q_{95} \gtrsim 5$. This higher q_{95} is less compatible with gaining access to ohmic H-mode plasmas for MLP operation, which

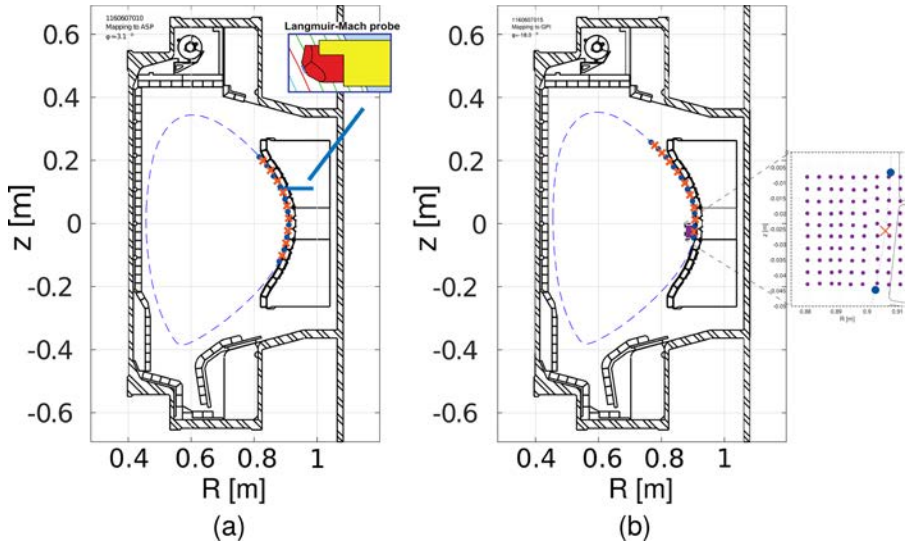

Figure 3. (*a*) The mirror Langmuir probe and (*b*) the 9 × 10 array of GPI focal spots, shown in their poloidal cross sections together with the LCFS (dashed blue line) and the locations of the field lines on the LCFS passing in front of antenna rungs (×'s and •'s).

favor $q_{95} \sim 3$ for transition to H-mode. Moreover, at all operationally-available q_{95} values, the mapped rungs completely missed the GPI views and the reflectometer array.

However, at the new location, the antenna rungs map to the MLP at essentially all attainable q_{95} values, as well as GPI and reflectometry, giving three independent measurements of the driven mode's radial profile.

2.2. Fluctuation diagnostics

The Mirror Langmuir Probe (MLP [14, 23]) cycles through three bias states in ∼0.9 μs, which enables it to resolve fluctuations of practical interest for electron density, n_e, electron temperature, T_e, and plasma potential, Φ, over the span of the profile obtained by scanning the reciprocating probe head. Profiles are obtained *for the same scan* by smoothing over the measurements. The scan velocity is typically between 0.4 and 0.5 m s^{-1}, except at the rapid turnaround at maximum insertion [27]. The procedure followed here for inferring plasma potential, Φ, and electron density and temperature, n_e and T_e, from MLP data is as described in section II.c of [14], except that the secondary electron emission coefficient is calculated in accordance with the guidelines provided by Tolias [28, 29].

Figure 3(*a*) shows the MLP in its poloidal cross section, together with the locations of field lines passing in front of antenna rungs.

The gas puff imaging diagnostic (GPI, [13, 30, 31]) images edge fluctuations in a region that is toroidally-localized by the use of a jet of helium gas puffed radially from a nozzle about 3–4 cm outside the LCFS and 2.5 cm below the midplane. The GPI focal spots lie on a poloidal plane in a grid with 9 radially-separated columns and 10 vertically-separated rows with roughly uniform ∼4 mm spacing; this plane is shown in figure 3(*b*), together with the mapped antenna rung positions. The spot size in the focal plane is about 4 mm in diameter [13]. However, additional factors influence the true resolution of the system. For example, the toroidal extent of the puff is 15–20 mm [30]. As such, a larger flux tube is intersected by each viewing volume. Moreover, the view is purely toroidal, and so the focal plane is not orthogonal to the background field lines.

A reflectometer array is also available at static frequencies of 50, 60, 75, 88, 112, 132, and 140 GHz [25, 32], although, typically, only the lower five frequencies are of use in resolving the driven mode's radial profile. The analysis procedure used for reflectometry data is described in appendix A.2.

Mirnov coil data are also presented, particularly from coils that are situated under limiter tiles and are especially close to the plasma.

A fluctuation signature appears on other diagnostics, including two-color interferometry, though these data are not presented here.

Data for these fluctuation diagnostics are acquired at varying sampling rates—2 MHz for reflectometry and GPI, ∼1.1 MHz for the MLP, and 5 MHz for the Mirnov coils—and with varying triggers and sample windows. These timebases are aligned with the use of a global synchronization signal recorded on the digitizers of each diagnostic [33].

2.3. Power system

The power available to the Shoelace antenna was increased from 2 kW in the original configuration [21, 22] to 8 kW, replacing two T&C AG1010 amplifiers with two Tomco BT04000-AlphaA amplifiers. This doubled the antenna current, and hence the vacuum field perturbation induced by the antenna, from maximum peak and pulse-averaged values of ∼85 and 77 A in 2012 to 162 and 144 A in 2016. The overall improvement is illustrated in figure 4, which compares five power system metrics for typical discharges from the 2012 and 2016 campaigns.

2.4. Plasma discharge

In the following, consistent with typical nomenclature, the phrase, ELM-free H-mode, will be used to refer to non-EDA,

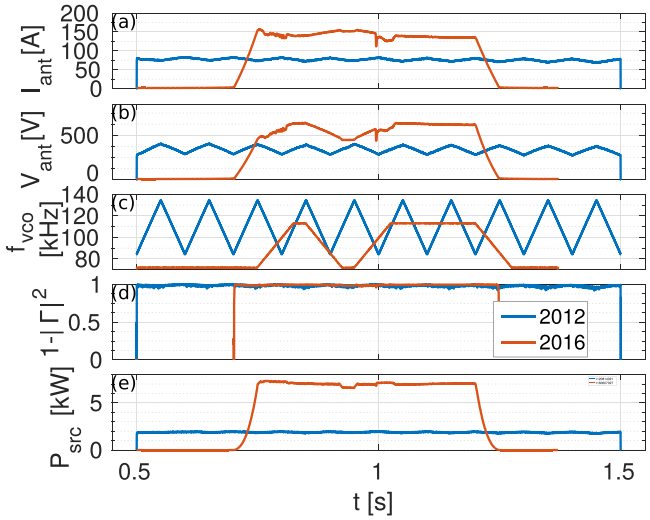

Figure 4. Comparison of Shoelace antenna power system performance metrics—(*a*) current through antenna winding, (*b*) voltage across winding, (*c*) frequency, (*d*) power fraction entering matching network, and (*e*) total source power—from two typical discharges, one from the 2012 campaign (blue), and one from 2016 with upgraded power system (orange—this is the same discharge as in figure 6(*b*)).

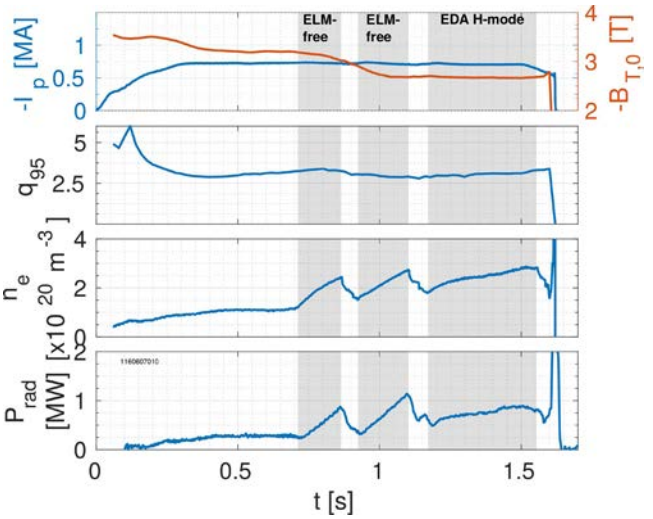

Figure 5. Parameter traces from discharge in 2016 Shoelace antenna campaign with three ohmic H-modes: 1st ELM-free, 2nd ELM-free with incipient QCM, 3rd EDA.

transient H-modes, distinct from steady-state EDA H-modes, though it should be pointed out that usually, EDA H-modes are also without ELMs.

The selection of discharge parameters for Shoelace antenna experiments is strongly constrained by the antenna's design. The antenna couples inductively to the plasma; since it is wound to match the QCMs perpendicular wavenumber, $k_\perp \approx 1.5$ cm^{-1}, its vacuum-field perturbation falls off as $\sim e^{-r/\ell}$, with $\ell = \frac{2}{3}$ cm and r the distance from the antenna winding. As such, for good coupling, the gap between plasma and antenna was minimized. This requirement is incompatible with high auxiliary heating power, especially with low density in the edge, since the resulting fast ion population can catastrophically damage the antenna winding. However, the plasma response to the antenna only exhibits a density fluctuation, and a resonance, in H-mode; in L-mode, only a perturbation in $\tilde{B}_\theta$ is detectable [20].

As such, a discharge must be selected that (*a*) gives access to H-modes (ELM-free or EDA), but (*b*) does not endanger the antenna or the MLP by the application of high auxiliary heating and a small outer gap. One scenario that satisfies these requirements is to reduce the H-mode power threshold such that it may be traversed with only ohmic heating. Ohmic H-mode is typically accessible at $q_{95} \lesssim 3$, as discussed in section 2.1.

Figure 5 shows parameter traces from one such ohmic plasma exhibiting three H-modes—two short-lived ELM-free phases and one long-lived EDA phase.

3. Results

Figure 6 shows spectrograms from two discharges in which the Shoelace antenna was energized. The signals displayed are from a Mirnov coil, a GPI view, and a reflectometer channel. Vertical lines mark transitions to confinement regimes (dashed), the times of MLP scans (dash-dot), and the end of the antenna power ramp down (white dashed). Each discharge exhibits both transient ELM-free as well as EDA ohmic H-modes, separated by short L-mode phases. In figure 6(*a*), the first two H-modes are transient ELM-free regimes without a QCM. In figure 6(*b*), the second H-mode is an EDA phase bearing a QCM. The antenna signature in these spectrograms is clearly distinguished as the narrow feature with a trapezoidal frequency trajectory. Importantly, the antenna frequency matches that of the intrinsic QCM at the time of the second MLP scan in the discharge shown in figure 6(b).

In the GPI and reflectometer spectra—and more generally, in spectra from diagnostics measuring density fluctuations—the Shoelace-driven fluctuation is only visible in H-mode, while the feature may appear in the Mirnov spectrum in L-mode, as well. This recovers the behavior reported previously [20], despite increased antenna power. The largest plasma response to the antenna occurs when the antenna's frequency overlaps with the intrinsic QCM band. Nonetheless, a strong and clear signature appears even in a quiescent edge plasma when no QCM is present. Note that the driven fluctuation appears later in the GPI spectrogram, since the gas puff does not start to enter the plasma until ∼0.81 s.

Figure 7 shows the power spectral density from the MLP from ten scans: eight into ELM-free plasmas, one into an EDA H-mode where the antenna frequency is just outside the QCM resonance, and another where the antenna frequency overlaps with the QCM. Antenna current varies between 105 and 142 A in the ELM-free cases, but there is little correlation between spectral power and antenna current. In the two EDA cases, I_A is between 134 and 136 A. The peak spectral power varies by a factor of two in the ELM-free cases, but is a factor of ∼40 greater in the EDA on-resonance case. The off-resonance EDA case exhibits a spectral power somewhat (∼50%) greater than the maximum level achieved in the ELM-free cases. Note that differences in amplitude correspond to the square root of those in spectral power.

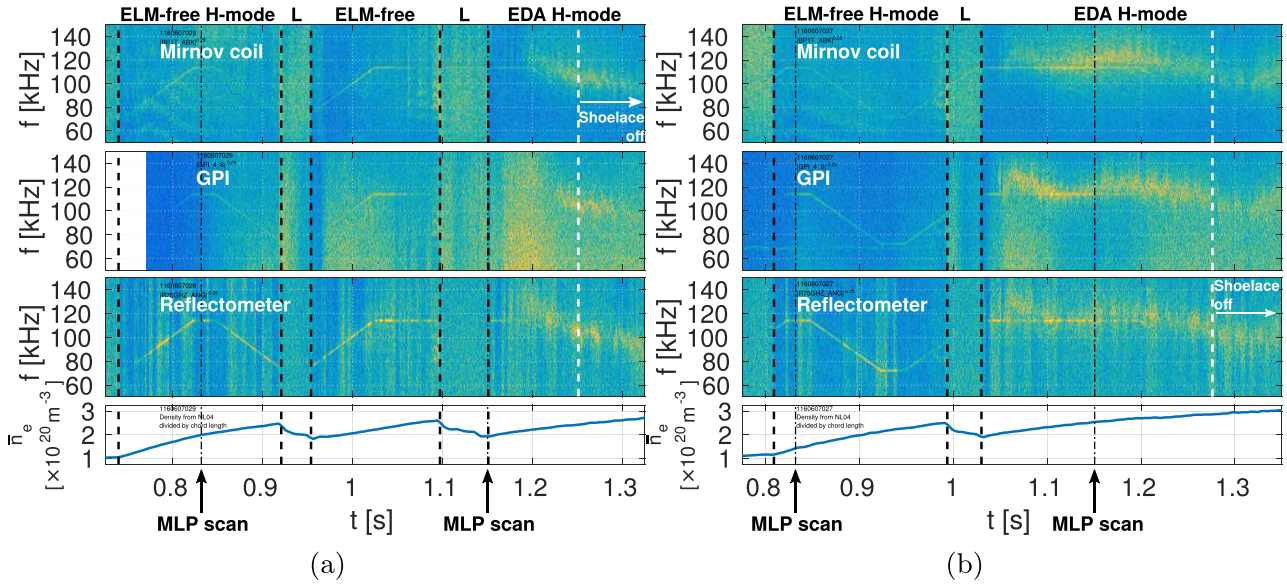

Figure 6. Spectrograms from a Mirnov coil measuring $\tilde{B}_\theta$, a GPI view, and the phase of the 75 GHz reflectometer channel, for (*a*) an antenna pulse that runs during two transient ELM-free H-modes, and ramps down just at the onset of an EDA H-mode, and (*b*) a pulse that overlaps with a long-lived, fully-developed EDA H-mode phase.

Because of the rapid variation in the background resonance frequency, it is not clear that the MLP scans sampled the plasma at times when the plasma response to the antenna was maximized. Nonetheless, it is clear that there is a substantial difference between the cases when the QCM and antenna frequencies overlap, and when they do not. Even when the antenna and QCM frequencies overlap, the antenna response is clearly discernible from the background QCM, likely because its coherence time is much longer. The integrated spectral energy under the narrow antenna peak in the MLP response is less than, but still comparable to, the energy contained over the QCM band, less the antenna feature. This separation of scales suggests that the signal processing techniques of appendix A.5 are capable of isolating transport correlated with the induced fluctuation from that driven by the background QCM.

The edge electron density and temperature profiles from these two discharges are shown in figure 8, with fits combining MLP and Thomson data using the modified hyperbolic tangent of equation (A.1), according to the procedure outlined in the appendix. The fit is shown by a thick black line, while the reflectometer cutoff densities are indicated by thin dashed black lines. The symbol, ρ, is the flux label, and corresponds to the distance along the major radius, relative to the LCFS, after mapping the measurement location to the outer midplane.

The profiles must be shifted to account for the error in the EFIT estimate for the location of the LCFS. The shift is calculated such that $\rho = 0$ aligns with the location in the profile fit corresponding to the temperature of the LCFS, as determined by power-balance. In particular, the temperature at the separatrix is inferred from the value required to account for the total power entering the scrape-off layer (SOL)—here, ohmic power less radiated power and change in stored energy—by Spitzer-Harm electron parallel heat conduction [34, section III.C]. Typically, the LCFS is between 40 and 60 eV (44 eV in figure 8(*a*), 56 eV in figure 8(*b*)).

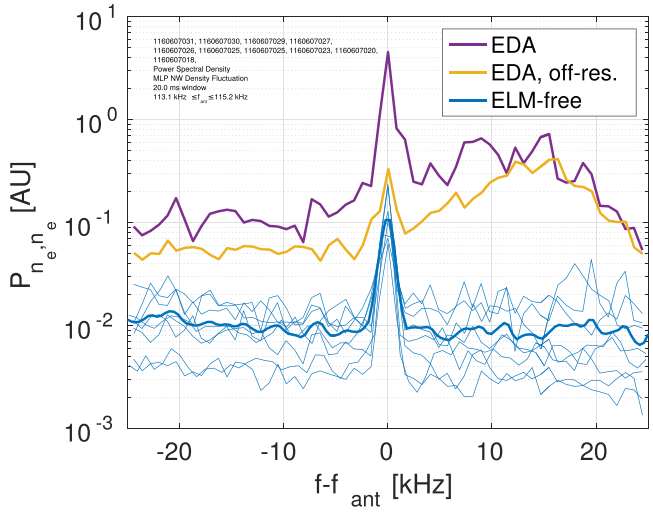

Figure 7. Power spectral density from MLP from 20 ms of data, using Welch's modified periodogram method averaging over 1.2 ms windowed, overlapping segments. Three scenarios are shown: an EDA H-mode with a QCM center frequency near the antenna frequency (purple line), an EDA H-mode where the antenna frequency is further from the QCM resonance (yellow line), and ELM-free cases (blue lines; thin lines corresponding to each of eight individual scans, and thick line the average over these). The plots are centered on the antenna frequency (here, between 113 and 115 kHz) for comparison.

3.1. Radial location of driven mode

The MLP, GPI, and reflectometry diagnostics are all capable of resolving the radial profile of the driven fluctuation. This can be done with the help of the magnitude squared coherence between the fluctuation signals and the antenna current, as well as the driven fluctuation amplitude estimated from the product of the transfer function (equation (A.5)), H_{xy}, and the antenna current, I_A.

The driven mode spatial profile from reflectometry is determined by inverting the density profiles at the plasma oscillation

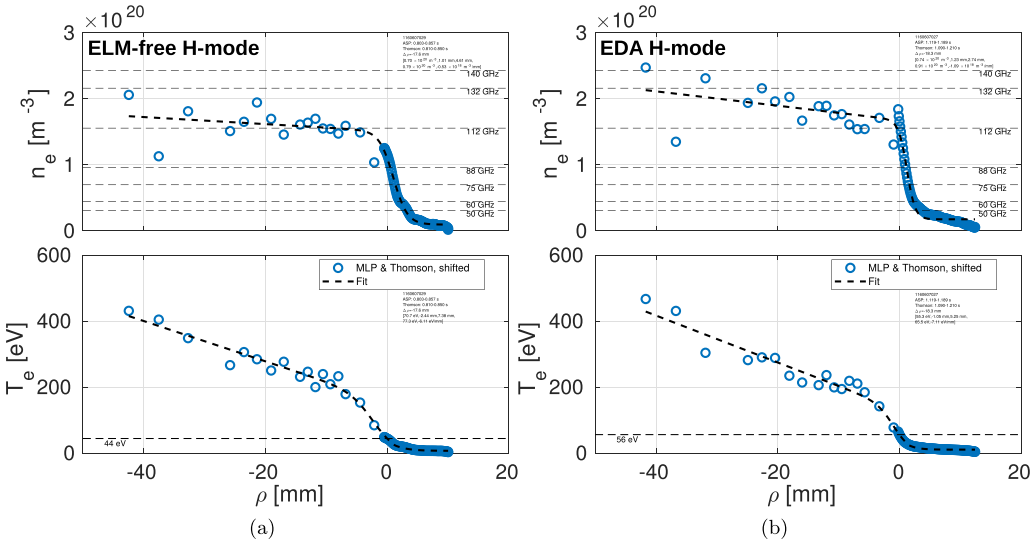

Figure 8. Profiles obtained by combining data from MLP scans with Thomson scattering for the discharges shown in (*a*) figure 6(*a*) (from the first MLP scan during the first ELM-free H-mode) and (*b*) figure 6(*b*) (from the second scan during the EDA H-mode).

cutoff densities. Absolute densities are estimated from geometric optics, equations (A.2) and (A.3). Because the timing of the transitions into H-mode varies unpredictably from one discharge to the next in these ohmic plasmas, the MLP samples the edge at different times in the profile evolution. One consequence of this is that, at MLP scan times, differing pedestal heights result in varied cutoff locations along the profile. Nonetheless, there are typically at least four reflectometer frequencies that cover the region near the separatrix.

Figure 9(*a*) is a two-dimensional, top-down view in the ρ, ϕ plane of the magnitude squared coherence between GPI signals and the antenna current from the ELM-free discharge shown in figure 6(*a*). Black circles depict the GPI focal points. These points are defined in the poloidal plane, but have been mapped to the outer midplane along field lines intersecting their measured (R, z) coordinates, adapting the 'ballooning' coordinate system [35, section 3.3], [36, section 3.5.1], except that the radial coordinate is represented by ρ rather than the poloidal flux. The cross coherence is interpolated from these mapped locations onto a rectangular ρ, ϕ grid to produce the contour plot. While the mapping utilizes the EFIT equilibrium, the ρ grid is ultimately shifted outward by $\sim$14 mm from its EFIT location to align the peak in the driven mode profile with that from the MLP. The cross-phase yields an estimate of the toroidal mode number of $n \approx 30$, consistent with $k_\perp \approx 1.5$ cm^{-1} in the EDD direction at the outer midplane. However, the two peaks in the $|C_{xy}|^2$ image have the same spacing as individual rungs on the antenna. The pattern of antenna rungs was also discernible from PCI measurements in previous experiments under off-resonance conditions [20, figure 11]. As such, in the cases that the antenna is either off-resonance or excites a weak resonance, the standing-wave character of the antenna-induced vacuum field perturbation is visible.

Figure 9(*b*) averages the interpolated values over ϕ to produce a radial profile of $|C_{xy}|^2$, using the vertical axis on the right. The same operation is applied to the estimate of the

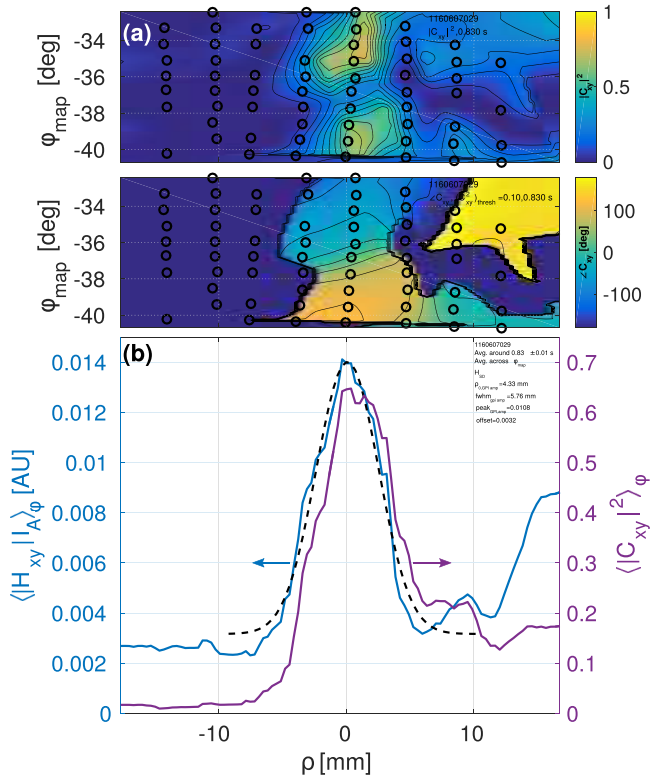

Figure 9. (*a*) Surface plots of $|C_{xy}|^2$ and $\angle C_{xy}$ (relative to I_A) obtained from GPI, mapped onto a ρ, ϕ grid. Black circles show mapped GPI focal points. $|C_{xy}|^2$ is derived from $\sim$20 ms of data around the first MLP scan time during an ELM-free H-mode (see figure 6(*a*), using Welch's modified periodogram method averaging over windowed, overlapping segments of 1.6 ms). (*b*) $|C_{xy}|^2$ and $|H_{xy}| \cdot I_A$, interpolated onto ρ, ϕ and averaged over ϕ to yield radial profiles. A Gaussian function with vertical offset is fit to $|H_{xy}| \cdot I_A$. (*a*) and (*b*) are shifted radially to align the GPI and MLP $|C_{xy}|^2$ profile peaks. The averaging process in (*b*) employs a discontinuous nearest-neighbor interpolation because it is better-behaved far from sample points, though a C^1 interpolation is used in plotting (*a*).

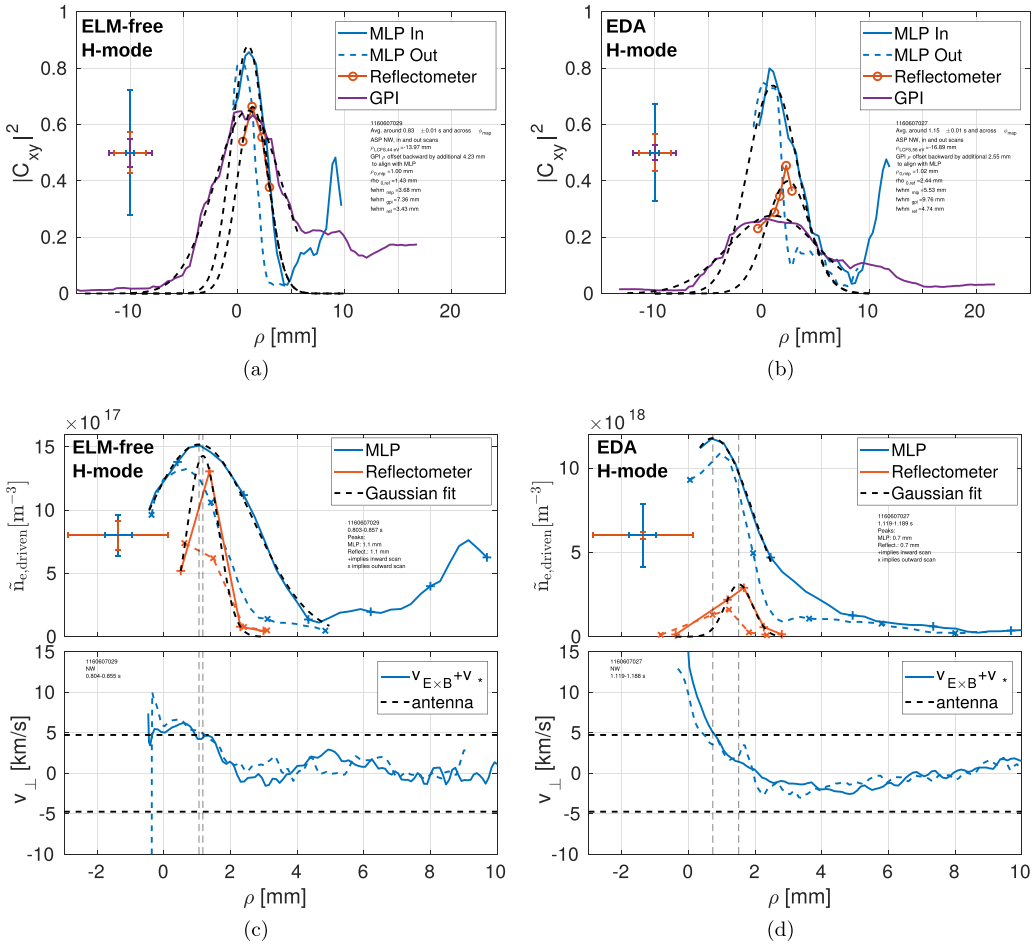

Figure 10. (*a*) and (*b*) Radial profiles of $|C_{xy}|^2$ for GPI (purple lines), MLP (blue lines), and reflectometer (orange lines and circles). (*c*) and (*d*) Estimates of the correlated fluctuation amplitude from $|H_{xy}| \cdot I_A$ for the MLP (blue) and reflectometer channels (orange). Black dashed lines show Gaussian fits. Time periods corresponding to inward MLP scans are shown with colored solid lines; to outward scans, colored dashed lines. (*a*) and (*c*) are from a transient ELM-free H-mode, while (*b*) and (*d*) are from an EDA H-mode. (*c*) and (*d*) also show the sum of the $\mathbf{E} \times \mathbf{B}$ and EDD velocities. The horizontal black dashed lines show the quotient of the antenna angular frequency and wave number; both the positive and negative values are shown because the antenna does not launch waves in a preferred direction. Vertical error bars correspond to a single data point—the peak—in a profile. For MLP and reflectometer, they represent only the standard error of the mean spectral estimates (in 1.6 ms bins for MLP, 20–30 ms bins for reflectometer); for GPI, only of the average over the flux surface. Horizontal error bars shown are, for MLP, $\pm\frac{1}{2} \times 0.5$ m s^{-1} plunge speed $\times$ 1.6 ms bin $\pm$ 0.4 mm; for reflectometer, $\pm\frac{1}{2}$ Airy width $= \pm 1.5$ mm (see appendix A.1), and for GPI, $\frac{1}{2}$ spot size $= \pm 2$ mm. Tables 1 and 2 provide a more complete characterization of uncertainty by tracking parameterizations of these profiles over multiple discharges and diagnostics.

driven mode amplitude given by the product, $|H_{xy}| \cdot I_A$; this is plotted against the vertical axis at left. The GPI data has been normalized by the background emission, determined by smoothing the GPI signal to remove fluctuating components. This is necessary because the GPI signal is proportional to the level of gas that has penetrated the viewing volume, which is neither spatially nor temporally stationary. The peaks in the $|C_{xy}|^2$ and $|H_{xy}| \cdot I_A$ profiles overlap closely, and share a similar full-width-at-half-maximum (FWHM) of 5–6 mm (recalling that the GPI spot size is about 4 mm).

Figure 10(*a*) combines the magnitude squared coherence profiles inferred from the GPI (purple lines), MLP (blue lines), and reflectometer (orange lines and circles) for a transient ELM-free plasma. Figure 10(*b*) does the same for an EDA discharge. Data from the inward and outward scans of the MLP are distinguished by solid (inward) and dashed (outward) lines; each point on the plot is derived from 1.6 ms of data, while the whole profile covers ~25 ms. The reflectometer and GPI profiles are constructed from 20–30 ms of data around the time of the MLP scan, with power spectra constructed by averaging over windows of 1.6 ms; the longer time blocks are possible since different spatial locations are sampled simultaneously and continuously. Figures 10(*c*) and 10(*d*) show the profiles of the amplitude estimates. The inward scan is shown as a dashed blue line with crosses, and the outer scan as a dashed line with $\times$'s. The reflectometer profile is shown in orange. Gaussian fits are shown as black dashed lines in both profile sets.

In the transient ELM-free case, figure 10(*a*), the MLP and reflectometer mode profiles overlay closely, peaking about 1 mm outside the LCFS. The GPI peak has been aligned with that of the MLP with the aid of the Gaussian fits. The MLP profile is slightly narrower than the GPI profile, while reflectometry suggests a still narrower mode layer.

In the EDA discharge, figure 10(*b*), the coherence registered by GPI drops considerably, and for the reflectometer to

Table 1. Radial structure of driven mode from profile of $|C_{xy}(\rho)|^2$.

Diagnostic	Regime	Driven mode FWHM $\pm 1\sigma$ (mm)	Driven mode $\rho_0 \pm 1\sigma$ (mm)	Peak $\lvert C_{xy}\rvert^2$
GPI	ELM-free	6.7 ± 0.78	N/A	0.51 ± 0.09
MLP	ELM-free	4.7 ± 1.1	1.1 ± 0.4	0.91 ± 0.04
Reflectometer	ELM-free	3.7 ± 1.2	1.7 ± 0.8	0.67 ± 0.08
GPI	EDA	9.8	N/A	0.28
MLP	EDA	5.5	1.0	0.74
Reflectometer	EDA	4.7	2.4	0.4

Table 2. Radial structure of driven mode from profile of $I_A\,|H_{xy}(\rho)|$.

Diagnostic	Regime	Driven mode FWHM $\pm 1\sigma$ (mm)	Driven mode $\rho_0 \pm 1\sigma$ (mm)	Peak $\tilde{n}_e \pm 1\sigma$ $(\times 10^{19}\ \mathrm{m}^{-3})$ $\left(\frac{\tilde{n}_e}{\bar{n}_e} \pm 1\sigma\,(\%)\right)$
GPI	ELM-free	5.5 ± 0.5	N/A	N/A
MLP	ELM-free	3.9 ± 0.6	1.3 ± 0.3	0.22 ± 0.05 ($2.5\% \pm 0.5\%$)
Reflectometer	ELM-free	1.6 ± 0.7	1.5 ± 0.5	0.13 ± 0.06 ($1.6\% \pm 0.8\%$)
GPI	EDA	5.0	N/A	N/A
MLP	EDA	2	0.7	1.4 (12%)
Reflectometer	EDA	0.96	1.5	3.1 (4.0%)

a lesser degree. All three diagnostics suggest a slightly wider mode layer. But the estimated mode amplitude is about an order of magnitude higher than in the ELM-free case.

Figure 10 also shows the profile of the sum of the $\mathbf{E} \times \mathbf{B}$ and EDD velocities, $\mathbf{v} = \mathbf{v}_{\mathbf{E}\times\mathbf{B}} + \mathbf{v}_*$, as determined by equation (A.8). In the EDA case of figure 10(*d*), for which the antenna frequency matches the intrinsic QCM, the location of the peak in the driven mode profile coincides with the point where the the sum of the ED and $\mathbf{E} \times \mathbf{B}$ drifts matches the phase velocity implied by the antenna frequency and wave number (shown by horizontal dashed lines). This is consistent with the idea that the antenna drives a drift wave resonance, with dispersion relation, $\omega = k_\perp v_*$, further Doppler shifted by the $\mathbf{E} \times \mathbf{B}$ velocity in the laboratory frame [20]. The same behavior also characterizes the intrinsic QCM [14]. It should be noted that the antenna does not launch waves in a preferred direction, since the current in the winding rises and falls essentially simultaneously everywhere, with alternating orientation, creating a standing-wave field perturbation. However, the driven wave, like the intrinsic QCM [14], has phase velocity in the EDD direction in both the laboratory and plasma frames, to the extent that the $\mathbf{E} \times \mathbf{B}$ velocity at the mode location may be determined by the MLP.

In the transient ELM-free case of figure 10(*c*), where there is no background QCM, the sum of $\mathbf{v}_{\mathbf{E}\times\mathbf{B}}$ and $\mathbf{v}_*$ still matches the EDD-directed phase velocity inferred from the antenna frequency and wave number. This supports the idea that a damped drift wave resonance still exists in the ELM-free case. However, a counter-example to this behavior exists wherein a driven mode profile is still resolved, but the sum of $\mathbf{v}_{\mathbf{E}\times\mathbf{B}}$ and $\mathbf{v}_*$ does not match the inferred phase velocity for the antenna-driven mode ($\sim$1 km s^{-1} versus $\sim$5 km s^{-1}). Caution should be exercised in the interpretation of these drift velocities, as discussed in appendix A.4.

It is interesting to observe that there is a small, but nonzero, fluctuation on the outer-most GPI channels well into the scrape-off layer which lags the fluctuation at the mode layer by $\sim$110°. The MLP data hint at the same feature in the outer portion of the scan. On some channels, these fluctuations appear to persist even in L-mode, perhaps shielding the fluctuation deeper into the plasma.

Table 1 compiles the parameters—the FWHM, location (relative to the LCFS), and height of the peak in the fit—of the Gaussian fits to the radial mode envelope for the $|C_{xy}|^2$ profile. Averages and standard deviations are reported for the set of eight ELM-free discharges shown in figure 7, and compared with the sole EDA 'on-resonance' case—the EDA off-resonance case is not included, its parameters similar to ELM-free cases. Table 2 reports parameters from fits to the profile obtained from the amplitude estimate, $|H_{xy}| \cdot I_A$[1]. To reduce the likelihood of errors due to probe tip melting, only data from the inward MLP scan are used in these tables.

The analysis employing $|C_{xy}|^2$ has the advantage of comparing the diagnostics on the same scale, and is less sensitive to difficulties in assessing absolute fluctuation quantities, particularly for reflectometry and GPI, but tends to produce a wider profile because the fluctuations at a given location may still be coherent with the driver, though greatly attenuated in amplitude. The profile of $|H_{xy}| \cdot I_A$, in principle, is more directly related to the quantity of interest—the driven mode amplitude—but is subject to greater uncertainties.

The reflectometer cutoffs are assessed from density profiles strongly weighted by MLP data in the region where the mode peak occurs; as such, the peak location determined from the reflectometer may be compared directly with that from the MLP. However, GPI peaks may not be independently aligned with those of the MLP and reflectometer due to EFIT errors in the GPI mapped radial location of $\sim$1 cm, and so they are not reported.

[1] For GPI amplitude fits, an additional vertical offset parameter is included, but is not recorded in the table, since the amplitude is not available in physical units.

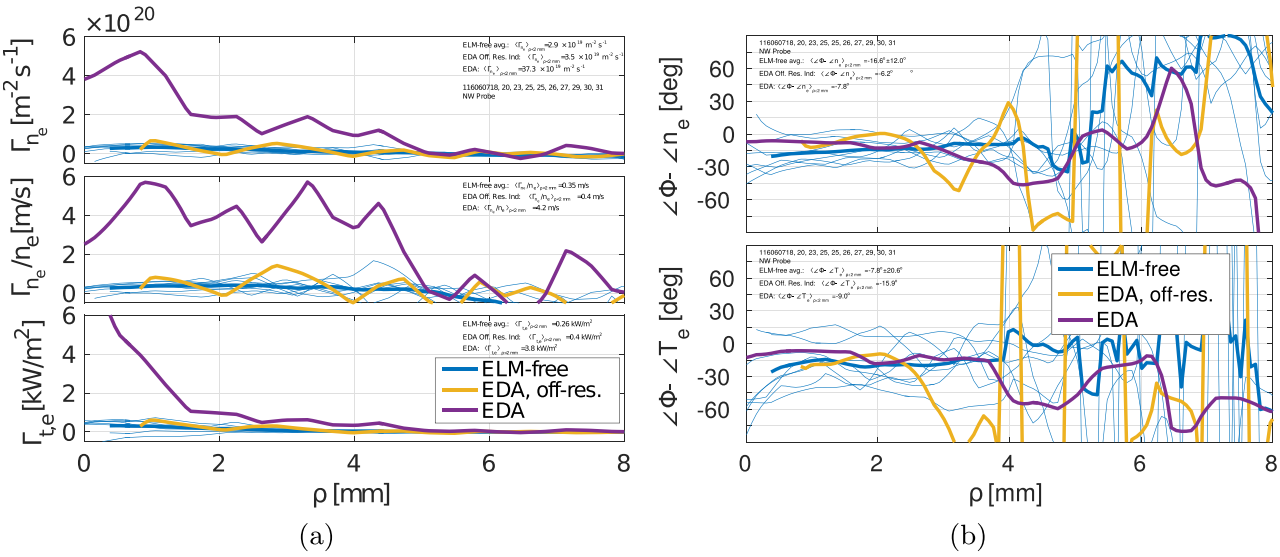

Figure 11. (*a*) Electron flux, Γ_{n_e}; convection velocity, Γ_{n_e}/n_e; and thermal flux convected by electrons, $\Gamma_{t,e}$, evaluated using equations (A.5) and (A.10). (*b*) Relative phase between transfer functions for the $\tilde{\Phi}$ and $\tilde{n}_e$ responses, as well as the $\tilde{\Phi}$ and the $\tilde{T}_e$ responses. Three scenarios are shown: an EDA discharge with the antenna on the QCM resonance (purple), an EDA discharge with the antenna off-resonance (yellow line), and a set of scans into eight ELM-free plasmas (thin blue lines), whose average is shown by a thicker blue line.

Before interpreting these results, it is appropriate to review the factors that determine the resolution of each diagnostic. The GPI signals integrate the plasma response over a volumetric region, as described in section 2.2. Along the same lines, the GPI focal point spot size of ∼4 mm limits the radial resolution of the diagnostic, and tends to smear out the profile over a broader radial region. The set of static reflectometer frequencies available gives only four to five measurements over the span of the mode layer, with radial spacing of cutoff layers typically ∼1 mm, depending on the profile, though the actual radial resolution of each reflectometer channel is likely wider than this, as described in appendix A.1. Moreover, the density response derived from reflectometer measurements suffers from uncertainties due to the crude geometric optics approximation, errors from inverting the density profile, and possible phase runaway. By comparison, the MLP provides the tightest radial resolution ($\lesssim$1 mm, given a 0.4–0.5 m s^{-1} scan velocity and 1.6 ms signal processing window length) and most unambiguous measurements, though it cannot be used to examine time evolution of fluctuations, nor can it penetrate more than several millimeters beyond the separatrix.

As expected, the average FWHM derived from $|H_{xy}| \cdot I_A$ is narrower than the $|C_{xy}|^2$ estimate. Moreover, the reflectometer profiles give the narrowest FWHM estimates, and GPI the widest. The reflectometry FWHM estimate in ELM-free H-mode from table 2 (1.6 ± 0.7 mm) is essentially identical to that reported for the QCM from a reflectometer study (1.0 ± 0.2 mm, [32, figures 5–12]), and the GPI FWHM (5.5 ± 0.5 mm) also recovers the estimated QCM width previously found by this diagnostic (∼5 mm, [13, p 1324]), as does the FWHM estimate from MLP (3.9 ± 0.6 mm in table 2 versus ∼3 mm in [14, figure 12]).

The MLP-derived radial location of the driven mode—spanning, and with peak very close to and just outside ($\rho \approx 1.3 \pm 0.3$ mm), the LCFS—is consistent with the behavior reported for the QCM from MLP studies [14, section E] using similar power-balance methodology to find the separatrix. The driven mode profiles from reflectometry place the fluctuation in essentially the same position ($\rho \approx 1.5 \pm 0.5$ mm). In the ELM-free cases, the peak locations given by mode amplitude depart only slightly from the corresponding $|C_{xy}|^2$ values, within a standard deviation from either data set.

The single 'on-resonance' EDA case exhibits more variation between diagnostics, as well as from the ELM-free averages, but it is not clear whether this is significant. Averaging over a larger data set, were one available, would likely reduce this disagreement.

3.2. Driven transport measurements

The transport correlated with the antenna-driven fluctuations may be inferred with the help of equation (A.10) or (A.13); these calculations are aided by the narrow bandwidth in frequency and $k_\perp$ imposed by the antenna. Figure 11(*a*) plots the electron flux, Γ_{n_e}; the electron convection velocity, Γ_{n_e}/n_e; and the electron convected thermal flux, $\Gamma_{t,e}$. These are the result of equation (A.10) for the transient ELM-free and EDA H-modes from figure 7, using equation (A.5) to evaluate the transfer function in the spectral domain at the antenna frequency. Three scenarios are shown, as in figure 7: an EDA case with the antenna frequency overlapping with the QCM band (the 'on-resonance' case, purple line), an EDA off-resonance case (yellow line), and a set of eight scans into ELM-free plasmas (thin blue lines, with a thick blue line showing their average). While the EDA off-resonance case has comparable transport to the ELM-free levels, it is apparent that the EDA on-resonance transport profiles have fluxes and particle convection velocity that exceed the off-resonance and ELM-free cases by an order of magnitude, as might be expected from the substantially-higher peak in the antenna response seen for the on-resonance case in figure 7.

Table 3. Fluctuation-induced transport correlated with antenna current.

Regime	$\Gamma_{n_e} \pm 1\sigma$ ($\times 10^{19}$/(m^{2}s))	$\Gamma_{n_e}/n_e \pm 1\sigma$ (m s^{-1})	$\Gamma_{t,e} \pm 1\sigma$ (kW m^{-2})	$\angle\tilde{\Phi} - \angle\tilde{n}_e$, $\angle\tilde{\Phi} - \angle\tilde{T}_e$ at Peak Loc.
ELM-Free	2.9 ± 1.9	0.35 ± 0.21	0.26 ± 0.27	$-16.6° \pm 12.0°$, $-7.8° \pm 20.6°$
EDA off-res.	3.5	0.4	0.4	$-6.2°$, $-15.9°$
EDA on-res.	37.3	4.2	3.8	$-7.8°$, $-9.0°$

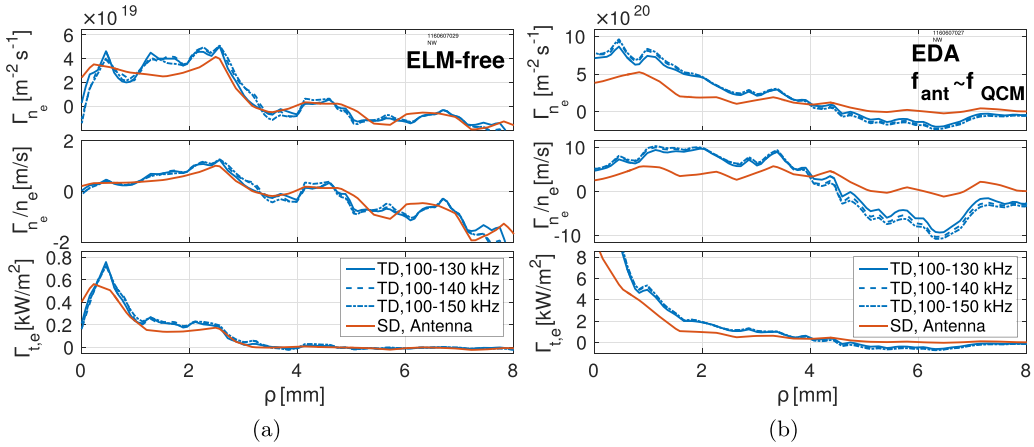

Figure 12. Comparison of transport evaluated from equation (A.10) (spectral domain, orange), computing fluxes correlated with antenna current, and (A.13) (time domain, blue), evaluating total fluctuation-induced flux in the indicated frequency bands.

It is germane in this context to discuss the relative phase between the $\tilde{\Phi}$ and $\tilde{n}_e$ signals, and between $\tilde{\Phi}$ and $\tilde{T}_e$. The relevant quantities for fluctuations correlated with the antenna current can be estimated from the phase difference between the transfer functions for each pair of quantities, $\arg\left(H_{\Phi,I_A} H^*_{n_e,I_A}\right)$ and $\arg\left(H_{\Phi,I_A} H^*_{T_e,I_A}\right)$, where the asterisk denotes the complex conjugate. When this phase difference is zero, there is no fluctuation-driven flux. Inside of $\rho = 4$ mm, over which range there is a higher degree of coherence between the antenna and the fluctuation signals, the relative phase settles to small values, with $\tilde{\Phi}$ lagging both $\tilde{n}_e$ and $\tilde{T}_e$ by $\sim 10°$. This reproduces the behavior of the QCM observed previously [14, figure 15]. The small relative phase lag further establishes the drift-wave-like character of these fluctuations [37, section IV], at least on open field lines, though MLP data has also suggested that there is a significant interchange component in the drive of the QCM [14, section V.A], as does the ballooning nature of the mode.

Table 3 compiles descriptive parameters from this analysis, reporting each quantity averaged between $0 \leqslant \rho \leqslant 2$ mm. Again, it is clear that convected quantities correlated with the antenna current are an order of magnitude larger in the EDA case relative to the ELM-free case. In the EDA case, the electron convection velocity, at 4.2 m s^{-1}, approaches the value of 10 m s^{-1} reported for the QCM [14, section IV.F].

Transport quantities were also evaluated using equation (A.7) to compute the transfer functions. Average quantities for transient ELM-free discharges at the peak location agree to better than $\sim 10\%$ between the two methods, with the exception of $\angle\tilde{\Phi} - \angle\tilde{T}_e$, which has a discrepancy closer to 15%. For the sole EDA on-resonance scan, the results at the peak location using the time-domain estimates for electron flux quantities exceed the spectral-domain estimates by $\sim 35\%$.

Figure 12(*a*) plots the same transport profiles from a transient ELM-free discharge, while figure 12(*b*) shows the case of the antenna on-resonance during an EDA discharge. The transport evaluated from equation (A.10) (orange line) is shown alongside the result of the time-domain method, equation (A.13) (blue lines), which computes the total transport in the indicated frequency band, albeit with a fixed wavenumber matching the antenna. This compares the portion of fluctuation-induced transport correlated with the antenna to the total flow. In the ELM-free case, the antenna-driven perturbation appears to account for most of the net fluctuation-induced transport between 100 and 150 kHz. In the EDA case, the QCM, which occupies the band between 105 and 140 kHz, contributes to outward particle and thermal flows, but the antenna-correlated fluctuations still provide a significant component of total transport. The 10 m s^{-1} convection velocity reported for the QCM in [14, section IV.F] matches the cumulative transport level (antenna-correlated and intrinsic QCM) given by this time-domain calculation. Recall that the spectral energy under the antenna signature contained in the MLP $\tilde{n}_e$ power spectrum from the EDA case, figure 7, is a little more than half that of the QCM (after removing and interpolating over the narrow antenna frequency band).

3.3. Driven mode is toroidally localized, with ambiguous effect on global confinement

Given the quadrupling in antenna power, it is appropriate to revisit the antenna's capacity to effect a global perturbation in the plasma, both with regard to the spatial extent of the driven fluctuation, as well as its impact on global equilibrium parameters.

Consider figure 13, which estimates the time-varying driven mode amplitude measured by a Mirnov coil via the product,

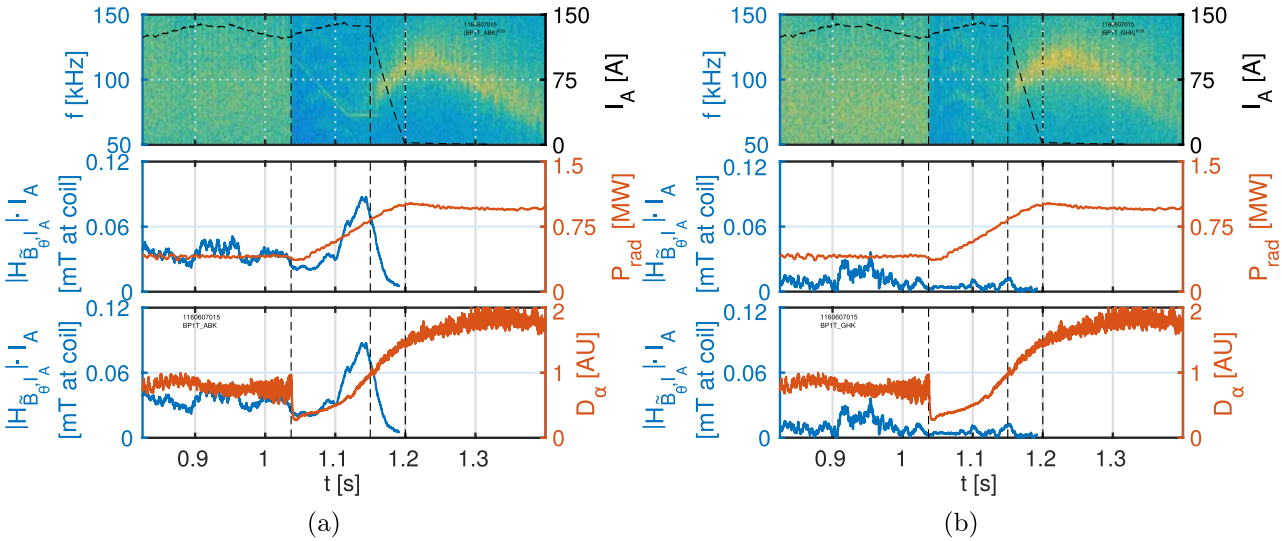

Figure 13. (*a*) Stacked plot of Mirnov coil spectrogram, overplotted with I_A on right-axis; followed by plot of $\left|H_{\tilde{B}_\theta,I_A}\right| \cdot I_A$ overplotted with P_{rad}; and then, the same driven $\tilde{B}_\theta$ amplitude estimate together with D_α emission. (*b*) The same set of plots using fluctuation data from a Mirnov coil that does not map to the antenna.

$|H_{yx}| \cdot I_A$. This is plotted together with traces of radiated power, P_{rad}, measured by a foil bolometer, as well as a signal proportional to D_α emission. Spectrograms from the two coils are also shown, as well as the antenna current amplitude to indicate when the antenna pulse ramps down. The fluctuation data in figure 13(*a*) come from a Mirnov coil which maps to the antenna; the coil that provided the data in figure 13(*b*) does not map to the antenna. Both coils show a sharp L-H-mode turbulence transition, a QCM with boomerang-shaped frequency modulation, and a set of four harmonics of a weaker, lower-*n* fluctuation that are not uncommon in these transient ELM-free ohmic H-modes[2]. However, while there is a prominent antenna signature in the spectrogram of the mapped coil, visible as the narrow feature with downward-sweeping and then constant frequency, no such signature appears on the unmapped coil.

Figure 13(*a*) indicates that the driven perturbation amplitude peaks just before the onset of EDA H-mode, perhaps because an intrinsic resonance slides through the antenna frequency at this time. Within a few milliseconds of the time that this peak occurs, (*a*) the intrinsic QCM appears and (*b*) the Shoelace antenna begins its power ramp down. Prior to the appearance of the QCM, the D_α emission begins to increase; the break-in-slope appears to coincide with an increase in the plasma response to the antenna. The radiated power does not roll over until after the intrinsic QCM appears, though a delay on the order of a confinement time between the QCM onset and the response in P_{rad} is both expected and observed, allowing the plasma's impurity inventory to adjust.

However, figure 14 appears to show a counter-example to the antenna's capacity to affect D_α emission. The data format in figure 14(*a*) is the same as in figure 13, with fluctuation data from the same mapped Mirnov coil. The time window samples a transient H-mode that exhibits an incipient QCM, but does not develop into a steady-state EDA H-mode. The antenna frequency sweeps across this weak background fluctuation twice, with the driven mode amplitude peaking by a factor of ∼3–4 around the resonance frequency, achieving a similar magnitude to that seen in figure 13(*a*). Despite this, there is no clear change in either P_{rad} or D_α.

Figure 14(*b*) presents data from a GPI view, rather than a Mirnov coil, and subtracts a linear trend from the P_{rad} and D_α signals to help reveal any correlation with peaking plasma response. Again, no such correlation is apparent.

4. Discussion: the Shoelace antenna and active edge control

Having characterized the antenna-induced fluctuation, we have established that the driven mode resembles the intrinsic QCM: it occupies the same narrow region of space around the LCFS, has only a ∼10° lag between $\tilde{\Phi}$ and $\tilde{n}_e$, as well as $\tilde{\Phi}$ and $\tilde{T}_e$, is field-aligned, has phase velocity in the EDD direction in both the laboratory and plasma frames according to MLP measurements, has outward particle and thermal flows, and matches the QCM $k_\perp$ and frequency range by design.

Interestingly, even in transient ELM-free plasmas without a background QCM, the antenna still drives a qualitatively-similar plasma fluctuation over a broad frequency range, albeit at lower amplitude. Moreover, the driven mode is not global, but guided by field lines and localized to the flux tube around the LCFS that passes in front of the antenna rungs. For comparison, however, the magnitude squared coherence of the intrinsic QCM—as measured between pairs of Mirnov coils at roughly the same poloidal, but different toroidal, positions—falls to zero at ∼25° of toroidal separation. Given a toroidal mode number, $n \sim 30$–35, for these low-q_{95} plasmas, this corresponds to ∼2–2.5 wavelengths. As such, the QCM perpendicular coherence length is short, as is the coherence

[2] See also figure 6. These modes are typically mutually-exclusive with the QCM, and are not thought to greatly impact edge transport given the transient nature of the H-modes in which they are found.

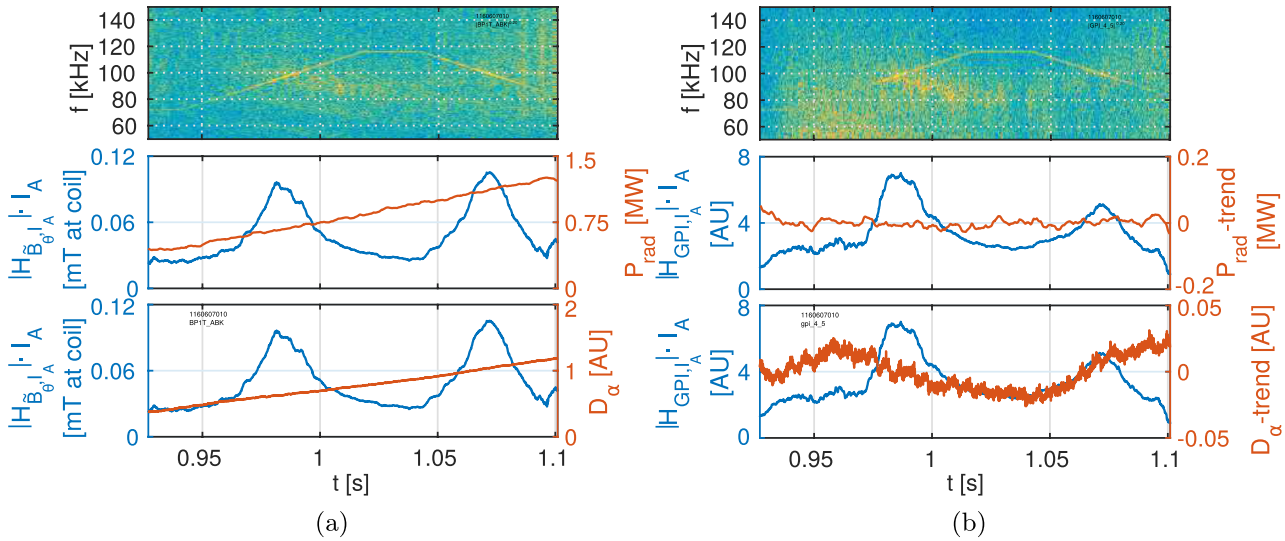

Figure 14. (*a*) Stacked plot with the same format, and using the same coil, as figure 13(*a*). (*b*) Another such stacked plot, but with fluctuation data obtained from a GPI view, and with linear trends in P_{rad} and D_{α} emission subtracted.

time, suggesting intermittency and localization in the intrinsic mode.

With this comparison in mind, we may discuss a principal motivation of this work: the possibility of exciting edge fluctuations to actively regulate impurity exhaust. Two questions that arise in this discussion are:

- At what level does transport associated with the induced fluctuations saturate with respect to increasing external drive?
- Does transport correlated with antenna-induced fluctuations enhance flow across the boundary, or does the plasma compensate by reducing other transport processes, clamping the total exhaust?

The first question might be addressed by examining the plasma response to the antenna at different power levels. Given the variation in this response, as well as the limited number of scans under relevant conditions, it is difficult to identify trends with antenna power using the MLP data presented in the previous sections. However, fluctuation amplitude might be used as a proxy for driven transport; these data are available over a much larger set of discharges and plasma scenarios, and may be better conditioned by averaging spectra over longer time segments. This analysis assumes that amplitudes of different fluctuating quantities are correlated, and the relative phase between them is fairly fixed.

Figure 15 plots the driven mode amplitude observed on a Mirnov coil, as inferred from the product, $\left|H_{\tilde{B}_{\theta},I_{\mathrm{A}}}\right| \cdot I_{\mathrm{A}}$, against antenna current. Each data point represents the maximum driven amplitude over an entire discharge. This is meant to improve uniformity in the data set, given the non-stationarity in the plasma response and variety of plasma conditions. Data points are categorized as either occurring at a time when the antenna frequency overlaps with a background QCM (orange squares), or when the antenna frequency is either far-removed from the QCM or no QCM is apparent (blue circles). There is substantial scatter, especially when the antenna frequency sits near a background QCM spectrum, since proximity to the QCM peak is not controlled here. Nonetheless, a statistically-significant correlation appears for both data sets, with the driven mode amplitudes about a factor of two higher in the on-background-QCM data set, on average. Also shown is the driven mode amplitude resolved during continuous upward and downward linear current ramps in a single discharge, with each ramp completed in ∼56 ms at a fixed frequency of ∼108 kHz. Again, the plasma response does not appear to saturate, but rather, to increase linearly in antenna current.

The second question—whether the driven fluctuations increase outward impurity flow—was addressed in section 3.3, which revealed ambiguity in correlating the driven mode with changes in signals associated with macroscopic confinement. We must consider whether driven fluctuations in these experiments were too small to measurably influence global confinement, or whether the plasma compensated by reducing other transport channels. Figure 11 suggests electron flux correlated with antenna-induced fluctuations is at least comparable to that of the background QCM on the flux tube that maps to the antenna, assuming we have successfully isolated the contribution from the antenna in the presence of a robust background QCM. However, the antenna rungs map to a toroidal range covering only about ∼100° over the outer midplane. As such, any locally-enhanced transport competes globally against the QCM with a factor of ∼3–4 handicap.

In the transient ELM-free case with a quiescent edge, the induced fluctuation amplitude is typically $\gtrsim$2–4 times below the level attained when the antenna frequency overlaps with the QCM, and correlated transport by the square of this value. This compounds the discrepancy in net global transport against the background QCM by an order of magnitude. As such, using the QCM scenario as a benchmark, and assuming additive contributions to flux, the transport due to the antenna in the ELM-free case is likely a factor of ∼30 below that of the QCM in an EDA H-mode. Detecting adjustments to macroscopic confinement parameters at this level is challenging, and so it is difficult to determine whether outward fluxes induced by the driven mode add to or are balanced by reductions in flows from other processes.

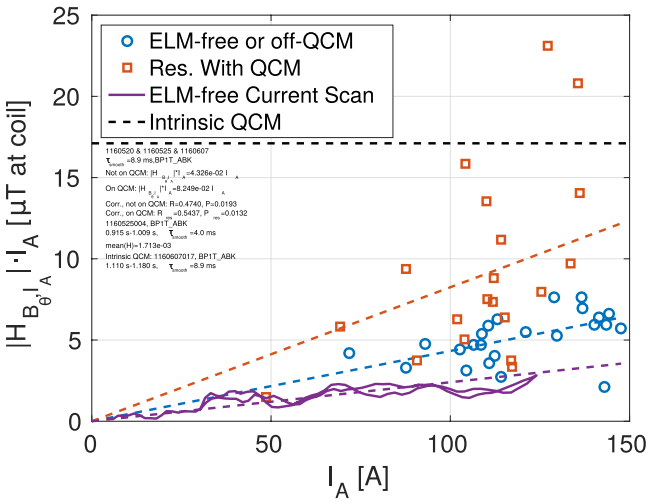

Figure 15. Each circle and square shows maximum Mirnov response against corresponding I_A for one discharge; orange squares are instances where antenna frequency overlaps with background QCM band, while blue circles show off-resonance or ELM-free cases. Dashed trend lines average $\left|H_{\tilde{B}_\theta,I_A}\right| \cdot I_A$ over each data set. Solid purple line shows Mirnov response from a single discharge over ∼56 ms-upward and downward ramps in I_A. Dashed black line shows amplitude of an intrinsic QCM.

Extrapolating the linearity in the plasma response in figure 15 another half a decade in I_A (from ∼150 A to ∼0.5 kA), and with the addition of two similar antennas disposed uniformly around the torus (or a greater number of antennas with fewer rungs), it might be possible to approach EDA transport levels in a quiescent ELM-free plasma exclusively from transport resulting from the antenna-induced fluctuations. Using Shoelace antennas on C-Mod, this would require a total power investment of ∼200–300 kW, with the majority dissipated in the windings. More precise alignment of the antenna relative to limiters, as well as the ability to adjust the antenna's radial position between discharges, could allow for significant gain in the induced perturbation at the LCFS due to the rapid decay of the perturbation over the SOL, relaxing the power requirement. This extrapolation is naïve, however, in that we do not know whether the plasma response will saturate at drive levels above those accessed in experiments reported here.

It must be remembered, also, that the proximity of the inductive antenna to the plasma at the outer midplane makes the winding vulnerable to damage, especially from fast ions in lower-collisionality regimes. Indeed, the Shoelace antenna winding was severed at the midplane by melt damage in three of the five campaigns in which it was installed. This, combined with the probable need for active cooling, makes the inductive approach for exciting edge fluctuations unattractive at the reactor scale, except, possibly, for low-mode-number oscillations along the lines of another active edge control scheme: resonant magnetic perturbation coils [38]. Instead, non-inductive means of exciting a fluctuation should be explored for active edge control (AEC). One such implementation might take the form of an array of electron-cyclotron-current-drive (ECCD) horn antennas, with amplitude modulation at the target mode frequency, where the amplitude modulation is phased across the array to produce the appropriate wave number [22]. This assumes a structure of helical current filaments spreading along field lines from a localized ECCD deposition spot, reproducing the mirror currents created by the Shoelace antenna. Such a filamentary model has been used to investigate the stabilization of neoclassical tearing modes (NTMs) by ECCD [39, sections II and III]. Critical to this scenario is the time scale over which such filaments evolve in response to RF deposition. Amplitude modulation of gyrotron sources has been studied extensively in support of NTM stabilization on ITER [40], with full power modulation at 5 kHz demonstrated at 1 MW and 170 GHz [41].

A passively-stable regime that regulates impurity content without the need of an actuator is still preferable in the reactor scenario from the perspective of robustness. Only if such scenarios are unattainable in practice, are associated with substantially-reduced power yield, or are prone to drop-outs resulting in the need for occasional feedback, would the development of AEC for a reactor be warranted.

From a scientific perspective, AEC experiments can test the understanding of mechanisms by which steady-state, ELM-free regimes exhaust impurities. In the present context, this means evaluating the idea of a soft transition between ELM-free and EDA H-mode, with the critical parameter along the transition provided by the QCM amplitude. This transition has been established for the QCM on Alcator C-Mod by correlating proxies for macroscopic confinement against mode amplitude ([10, figure 7], [13, figure 1]), and by inferring global transport levels from local measurements made by scanning Langmuir probes [11, 14]. Cases of QCM fluctuations apparently of insufficient magnitude to achieve a steady-state EDA H-mode were also observed on DIII-D with neutral-beam fueling [42, figure 11]. The ability to reproduce the macroscopic confinement characteristics of these regimes by externally-driven fluctuations would validate this conceptual understanding, while the converse would provide new insight into the role coherent edge fluctuations play in steady-state, ELM-free regimes, and what fluctuation properties are critical to this role.

From an active MHD perspective [43, 44], a device at the scale of the Shoelace antenna is useful to align radial profiles of fluctuation diagnostics, and to establish field-line-mapping between fluctuation diagnostics due to the narrowness of the flux bundle upon which the driven mode sits. The antenna also provides a means to benchmark simulations of a target mode (here, the QCM), due to the well-defined frequency and wavenumber of the driven perturbation, as well as the long spatial and temporal coherence. Comparing responses of antennas on the high- and low-field-sides can further assess the importance of curvature drive. Conversely, a clearer picture of the physics behind the driven mode could allow diagnosis of the edge plasma from measurements of a fluctuation driven at a non-perturbative level.

5. Conclusion

This work has reported the first direct measurements of fluctuation-induced transport correlated with the mode driven by the Shoelace antenna, and has also provided a characterization

of the driven mode's radial profile. These measurements were made possible by translating the antenna toroidally from its original location, so that the flux bundle mapping to the antenna on the LCFS passed in view of the set of relevant diagnostics. The study further benefited from a fourfold expansion of antenna power.

In both transient ELM-free and steady-state EDA H-modes, the antenna drives a fluctuation that matches the QCM in radial envelope and location ($\sim$4 mm FWHM and peak $\sim$1 mm outside the LCFS), as well as laboratory and plasma-frame phase velocities (following the drift-wave dispersion relation in both cases, according to MLP measurements). By design, the antenna's wave number and frequency range overlap with those of the QCM. Moreover, both the intrinsic and driven modes exhibit a small ($\sim$10°) lag between the plasma potential and electron density and temperature phase angles, $\angle\tilde{\Phi} - \angle\tilde{T}_e$ and $\angle\tilde{\Phi} - \angle\tilde{n}_e$—another drift-wave-like characteristic. Relative to the ELM-free or off-resonance cases, the amplitude of the driven mode increases by a factor of $\gtrsim$3 when its frequency overlaps with an intrinsic QCM, with driven transport following the square of the amplitude. In the on-resonance condition, the local electron particle and thermal fluxes correlated with the antenna-induced fluctuation are comparable to flows from the intrinsic QCM; the total spectral energy of the driven mode and QCM are also comparable. Nonetheless, due to the fact that only $\sim\frac{1}{4}$ of field lines at the outer midplane pass in front of the antenna, with a further reduction in coupling resulting from the non-conformity of the antenna shape to the plasma, and given the non-stationarity of both the plasma response and the QCM, it is difficult to distinguish a global effect of the antenna on macroscopic confinement, if it exists, from the effects of the intrinsic QCM. In the quiescent ELM-free case, with no background QCM, the antenna's capacity to affect global confinement is still ambiguous, given the reduction in driven mode amplitude—local measurements, as well as the antenna's limited toroidal reach, would suggest a $\gtrsim$30$\times$ reduction in driven transport in ELM-free H-mode relative to flows associated with the global, intrinsic QCM in EDA H-mode.

Despite wide variation, it appears that the plasma response scales approximately linearly with antenna current, or, at least, that the driven mode amplitude has not saturated at the levels of I_A achieved in these experiments. If this response is extrapolated, then total driven transport levels by the antenna obtained in quiescent ELM-free H-mode might approach the level of the intrinsic QCM with the addition of two more antennas disposed toroidally around the vessel, and a further order of magnitude expansion of input power at each antenna. More precise radial alignment of the antenna, as well as the ability to maximize the antenna response through feedback control of frequency, might reduce the power demand.

However, the inductive scheme to excite edge fluctuations pursued by the Shoelace antenna was meant to be a proof-of-concept study in active edge control; it does not extrapolate to a reactor scenario, except possibly for coupling to edge modes with low toroidal mode number. Instead, non inductive scenarios for exciting edge modes are desirable. Moreover, a confinement regime whose impurity content is passively-regulated by intrinsic plasma processes is clearly preferable to the actively-controlled case, should such regimes be accessible and of satisfactory performance.

In support of developing such passively-regulated scenarios, AEC experiments test the understanding of the role coherent edge fluctuations play in steady-state, ELM-free confinement regimes. While control of edge flows may be beyond the reach of smaller actuators on the scale of the Shoelace antenna, such actuators have an active MHD application, as the coherent features they drive allow for alignment of fluctuation diagnostics, facilitate benchmarking efforts for simulations of coherent edge modes, and, with an improved physics basis of driven modes, can help to diagnose the edge.

Acknowledgments

The authors gratefully acknowledge the effort of the Alcator C-Mod team in realizing the Shoelace antenna project over many years—especially D. Arsenault, A. Binus, D. Bellofatto, J. Bosco, W. Byford, C. Cauley, J. Chicarello, T. Fredian, D. Henshaw, M. Iverson, F. Kreisel, R. Murray, A. Pfeiffer, R. Rosati, M. Silveira, J. Stillerman, D. Terry, T. Toland, D. Tracey, B. Wood, and many others without whom these experiments would not have been possible. The authors are also thankful for insightful discussions with, and encouragement from, Prof. B. Coppi, Prof. R. Goldston, Dr. A. Hubbard, Dr. Y. Lin, Prof. C. Theiler, Prof. A. Fasoli, and Prof. R. Temkin. This work was supported by USDoE Coop. Agreement DE-FC02-99ER54512 and DE-SC0014264.

Appendix. Analysis procedure

A.1. n_e and T_e profiles

Profiles of electron density, n_e, and temperature, T_e, are synthesized by combining MLP and Thomson data in a fitting process employing a modified hyperbolic tangent function [45], constructed as

$$Y = \begin{cases} A\tanh\left[\frac{2(\rho_s-\rho)}{w}\right] + B & \text{if } \rho \geqslant \rho_k \\ A\tanh\left[\frac{2(\rho_s-\rho)}{w}\right] + B - s\cdot(\rho_k-\rho) & \text{if } \rho < \rho_k \end{cases} \quad \text{(A.1)}$$

where ρ is the distance from the LCFS at the midplane, ρ_s the symmetry point in the profile, w the width of the pedestal region, s the slope of the profile inside the pedestal, and ρ_k the knee of the profile at the transition between the steep gradient region and the inner, shallow-gradient region.

An additional free parameter was used to align Thomson and MLP data, in the form of an offset, $\Delta\rho$, subtracted from the Thomson n_e and T_e radial coordinates. This allowed the Thomson profiles to slide radially relative to those of the MLP during least-squares fitting.

A.2. Reflectometer geometric optics approximation

For direct comparison with MLP measurements, density fluctuation amplitudes were inferred from reflectometer measurements using geometric optics to estimate the

displacement, $\tilde{\delta}$, of the reflectometer cutoff layer [25, section 2.2.3], [32, section 3.1.1]. Under this approximation, $\tilde{\delta}$ is found from the phase angle, $\tilde{\alpha}$, obtained from the reflectometer I/Q detector,

$$\tilde{\delta} = \frac{\tilde{\alpha} c_0}{4\pi f_R} \tag{A.2}$$

with f_R the reflectometer frequency and c_0 the free-space speed of light, and where the measurement is localized to the point on the density profile where f_R matches the electron plasma frequency, $(2\pi f_R)^2 = \omega_{pe}^2 = \frac{n_e e^2}{\epsilon_0 m_e}$. Then $\tilde{n}_e$ is calculated from the local density gradient in the limit of small displacements:

$$\tilde{n}_e = \tilde{\delta} \nabla n_e. \tag{A.3}$$

An approximate lower bound for radial resolution can be estimated from a one-dimensional full-wave analysis [46, p 1233], [25, p 58,61], yielding the Airy width, $W_A = 1.63(L_n/k_0^2)^{1/3} = 0.479(c_0^2 L_n/f^2) = 2.14(L_n/f^2)^{1/3}$, with f the reflectometry frequency in GHz and $L_n = (\frac{\nabla n_e}{n_e})^{-1}$ the density scale length in mm; here, $L_n \lesssim 5$ mm, making $W_A \lesssim 3$ mm for the 50 GHz channel.

A.3. Signal processing

The cross-power spectrum, or cross-spectral density, is the Fourier transform of the correlation function [47, equations (1.24) and (1.34)],

$$P_{xy}(j\omega) = \int_{-\infty}^{\infty} \mathrm{d}t\, \mathrm{e}^{-j\omega t} \int_{-\infty}^{\infty} \mathrm{d}\tau\, x(\tau) y(t+\tau) \tag{A.4}$$

for two signals $x(t)$ and $y(t)$, and $P_{xy}(j\omega) = P_{yx}^*(j\omega)$. When $x = y$, the result of this operation is the autopower, P_{xx}.

The cross-power can be used to estimate both the transfer function [47, equation (1.43)],

$$H_{yx}(j\omega) = \frac{P_{yx}(j\omega)}{P_{xx}(j\omega)}, \tag{A.5}$$

and the cross-coherence [47, equations (1.38) and (3.65), [48, equation (7.6.13)],

$$C_{xy}(j\omega) = \frac{P_{xy}(j\omega)}{\sqrt{P_{xx}(j\omega) P_{yy}(j\omega)}}. \tag{A.6}$$

The latter quantity has the property that its magnitude is between 0 and 1. Often, it is the magnitude squared coherence, $|C_{xy}|^2$, that is displayed.

Unless otherwise noted, the auto- and cross-power are calculated here via Welch's averaged, modified periodogram method [49], implemented here by dividing a time series into segments with 50% overlap, with a Hamming window applied to each, and computing the average over the spectra of these segments. Standard error about the mean is considered, as well, in the construction of the error bars in figure 10. The cross-coherence and transfer function are then determined from these power spectra. For the MLP, the signal is typically divided into shorter time series of 1.6 ms to provide spatial resolution, with these series further split into 15 overlapping segments of 200 μs across which averages are computed; the exception is figure 7, where a 20 ms time series is used with windowed segments of 1.6 ms.

The transfer function can also be computed in the time domain via synchronous detection [50, 51] by

$$H_{yx}(t) = \frac{\mathrm{lp}\left\{\mathrm{bp}\left\{x(t) - j\mathcal{H}\left\{x(t)\right\}\right\} \cdot \mathrm{bp}\left\{y(t)\right\}\right\}}{\mathrm{lp}\left\{x^2(t)\right\}} \tag{A.7}$$

where $\mathcal{H}\{\}$ denotes the Hilbert transform [49], whose effect is to shift the phase of the signal it operates on by 90°, while $\mathrm{lp}\{\}$ denotes low-pass filtering with passband well under the drive frequency, and $\mathrm{bp}\{\}$ band-pass filtering with passband straddling the drive frequency and well above the $\mathrm{lp}\{\}$ passband. Synchronous detection is better-suited to narrow-banded functions, since the calculation convolves the spectral content across the passband of the $\mathrm{bp}\{\}$ filter; this constraint is comfortably satisfied by the antenna power system, which is essentially monochromatic.

In these experiments, the time and spectral domain methods for calculating H_{yx} agree when coherence is high between the antenna current and the fluctuation signal, with the discrepancy in magnitude estimates, $|H_{yx}|$, typically within 5%, and in phase angle, ±5°.

A.4. Drift velocities from MLP data

The $\mathbf{E} \times \mathbf{B}$ and electron diamagnetic drift (EDD) velocities, $\mathbf{v}_{\mathbf{E}\times\mathbf{B}} = \mathbf{E} \times \mathbf{B}/B^2$ and $\mathbf{v}_* = \nabla p_e \times \mathbf{B}/(n_e e B^2)$, can be calculated conveniently from MLP profiles; their sum is

$$\begin{aligned} \mathbf{v} &= \left(\frac{1}{n_e e}\frac{\mathrm{d}p_e}{\mathrm{d}\bar{\psi}} - \frac{\mathrm{d}\Phi}{\mathrm{d}\bar{\psi}}\right)\frac{\nabla\bar{\psi}\times\mathbf{B}}{B^2} \\ &= \left(\frac{1}{n_e e}\frac{\mathrm{d}p_e}{\mathrm{d}\bar{\psi}} - \frac{\mathrm{d}\Phi}{\mathrm{d}\bar{\psi}}\right)\frac{\nabla\psi\times\mathbf{B}}{(\psi_a - \psi_0)B^2} \end{aligned} \tag{A.8}$$

with $\bar{\psi} = \frac{\psi - \psi_0}{\psi_a - \psi_0}$ the normalized poloidal flux, where ψ_a is the flux at the separatrix and ψ_0 at the magnetic axis, and $\nabla\psi \times \mathbf{B} = \hat{R} B_R B_\phi R - \hat{\phi} R\left(B_z^2 + B_R^2\right) + \hat{z} R B_z B_\phi$ in cylindrical coordinates for the axisymmetric MHD equilibrium. Derivatives of equilibrium quantities with respect to $\bar{\psi}$ are determined via $\frac{\mathrm{d}u}{\mathrm{d}\bar{\psi}} = \frac{\mathrm{d}u}{\mathrm{d}t}/\frac{\mathrm{d}\bar{\psi}}{\mathrm{d}t}$ as the MLP scans through flux surfaces.

The calculation of the drift velocities is particularly sensitive, since it depends on gradients of profiles, with $\mathbf{v}$ the residue of two counter-propagating flows, and so care should be exercised when interpreting these results.

A.5. Driven particle and thermal fluxes from MLP data

The particle and thermal fluxes correlated with the antenna drive are calculated from the transfer function between the antenna current and the MLP n_e, T_e, and Φ traces. The flux expressions are derived starting from the time-averaged product of the quantity of interest with the radial drift velocity:

$$\Gamma_{n_e} = \left\langle n_e(t)\mathbf{v}_{\mathbf{E}\times\mathbf{B}}(t)\cdot\frac{\nabla\psi}{|\nabla\psi|}\right\rangle$$
$$\Gamma_{u} = \left\langle n_e(t)T_e(t)\mathbf{v}_{\mathbf{E}\times\mathbf{B}}(t)\cdot\frac{\nabla\psi}{|\nabla\psi|}\right\rangle. \quad \text{(A.9)}$$

The radial $\mathbf{E}\times\mathbf{B}$ velocity is produced by the fluctuating plasma potential, $\tilde{\Phi}(t)$. Let the complex phaser, $\tilde{A}$, of a monochromatic signal, $x(t) = A\cos(\omega t+\alpha)$, be defined through $x(t) = \Re\left\{\tilde{A}e^{j\omega t}\right\}$. We write the phasers of the fluctuating quantities correlated with the antenna drive as $\tilde{n}_e = H_{n_e,I_A}\cdot I_A$ and $\tilde{T}_e = H_{T_e,I_A}\cdot I_A$ and $\tilde{\Phi} = H_{\Phi,I_A}\cdot I_A$, where the transfer functions between these quantities and the antenna current are scaled by the antenna current amplitude to approximate the phaser values. The fluxes are then given by

$$\Gamma_{n_e} = -\frac{\hat{\mathbf{r}}k_\perp}{2B}\Re\{j\tilde{n}_e\tilde{\Phi}^*\} = \frac{\hat{\mathbf{r}}k_\perp}{2B}\Re\{j\tilde{n}_e^*\tilde{\Phi}\}$$
$$\Gamma_{u} = -\frac{\hat{\mathbf{r}}k_\perp}{2B}\Re\left\{j\left(\bar{T}_e\tilde{n}_e+\bar{n}_e\tilde{T}_e\right)\tilde{\Phi}^*\right\}$$
$$= \frac{\hat{\mathbf{r}}k_\perp}{2B}\Re\left\{j\left(\bar{T}_e\tilde{n}_e^*+\bar{n}_e\tilde{T}_e^*\right)\tilde{\Phi}\right\}. \quad \text{(A.10)}$$

Alternatively, the computation may be carried out in the time-domain via short-time-window-averaging. If $\Phi = \bar{\Phi}(r)+\Re\left\{\tilde{\Phi}(r)e^{j(\omega t-k_\perp y)}\right\}$, then $\nabla\Phi\cdot\hat{y} = \Re\left\{-jk_\perp\tilde{\Phi}(r)e^{j(\omega t-k_\perp y)}\right\} = k_\perp\Re\left\{\tilde{\Phi}(r)e^{-j\pi/2}e^{j(\omega t-k_\perp y)}\right\}$ $= k_\perp\mathcal{H}\{\tilde{\Phi}(t)\}$. Then, since

$$\mathbf{v}_{\mathbf{E}\times\mathbf{B}} = \frac{\mathbf{E}\times\mathbf{B}}{B^2} = -\frac{\nabla\Phi\times\mathbf{B}}{B^2} \quad \text{(A.11)}$$

and, taking care that the cross product of $\hat{\mathbf{y}}$ and $\mathbf{B}$ points outward radially,

$$v_r = -\frac{\nabla_y\Phi\times\mathbf{B}}{B^2} = -\frac{k_\perp\mathcal{H}\{\tilde{\Phi}(t)\}}{B}, \quad \text{(A.12)}$$

it follows that

$$\Gamma_{n_e} = \langle n_e v_r\rangle = -\frac{k_\perp}{B}\langle n_e(t)\mathcal{H}\{\tilde{\Phi}(t)\}\rangle$$
$$\Gamma_{u} = \langle n_e T_e v_r\rangle = -\frac{k_\perp}{B}\langle n_e(t)T_e(t)\mathcal{H}\{\tilde{\Phi}(t)\}\rangle \quad \text{(A.13)}$$

remembering that $n_e(t)$ and $T_e(t)$ are the *total* quantities, and not only the fluctuating components, while $\tilde{\Phi}(t)$ is high-pass-filtered to resolve the fluctuating quantity, only.

ORCID iDs

T. Golfinopoulos https://orcid.org/0000-0002-0898-5217
B. LaBombard https://orcid.org/0000-0002-7841-9261
D. Brunner https://orcid.org/0000-0002-8753-1124
J.L. Terry https://orcid.org/0000-0003-4255-5509
J.W. Hughes https://orcid.org/0000-0003-4802-4944

References

[1] Oyama N. *et al* (The ITPA Pedestal Topical Group) 2006 Pedestal conditions for small ELM regimes in tokamaks *Plasma Phys. Control. Fusion* **48** A171
[2] McDermott R.M. *et al* (Alcator C-Mod Team) 2009 Edge radial electric field structure and its connections to H-mode confinement in Alcator C-Mod plasmas *Phys. Plasmas* **16** 056103
[3] Whyte D. *et al* (The Alcator C-Mod Team) 2010 I-mode: an H-mode energy confinement regime with L-mode particle transport in Alcator C-mod *Nucl. Fusion* **50** 105005
[4] Burrell K.H. *et al* 2002 Quiescent H–mode plasmas in the DIII-D tokamak *Plasma Phys. Control. Fusion* **44** A253
[5] Burrell K.H. *et al* 2005 Advances in understanding quiescent H–mode plasmas in DIII-D *Phys. Plasmas* **12** 056121
[6] Kamiya K. *et al* (JFT-2M Group) 2004 High recycling steady H-mode regime in the JFT-2M tokamak *Plasma Phys. Control. Fusion* **46** A157
[7] Kamiya K., Oyama N., Ido T., Bakhtiari M. and (JFT-2M Group) 2006 Characterization of coherent magnetic fluctuations in JFT-2M high recycling steady high-confinement mode plasmas *Phys. Plasmas* **13** 032507
[8] Takase Y. *et al* 1997 High power density H-modes in Alcator C-Mod *Proc. 16th Int. Conf. on Fusion Energy (Montreal, Canada, 7–11 October 1996)* vol 1 pp 475–85 (https://inis.iaea.org/search/search.aspx?orig q=RN:28062985)
[9] Greenwald M. *et al* 2000 Studies of EDA H-mode in Alcator C-mod *Plasma Phys. Control. Fusion* **42** A263
[10] Hubbard A.E. *et al* 2001 Pedestal profiles and fluctuations in C-mod enhanced D-alpha H-modes *Phys. Plasmas* **8** 2033–40
[11] Snipes J., LaBombard B., Greenwald M., Hutchinson I., Irby J., Lin Y., Mazurenko A. and Porkolab M. 2001 The quasi-coherent signature of enhanced D_α H-mode in Alcator C-mod *Plasma Phys. Control. Fusion* **43** L23–30
[12] Mazurenko A., Porkolab M., Mossessian D., Snipes J., Xu X. and Nevins W. 2002 Experimental and theoretical studies of quasicoherent fluctuations in enhanced D_α plasmas in the Alcator C-mod tokamak *Phys. Rev. Lett.* **89** 225004
[13] Terry J. *et al* 2005 Transport phenomena in the edge of Alcator C-mod plasmas *Nucl. Fusion* **45** 1321–7
[14] LaBombard B., Golfinopoulos T., Terry J.L., Brunner D., Davis E., Greenwald M., Hughes J.W. and Alcator C-Mod Team 2014 New insights on boundary plasma turbulence and the quasi-coherent mode in Alcator C-mod using a mirror Langmuir Probe *Phys. Plasmas* **21** 056108
[15] Federici G., Loarte A. and Strohmayer G. 2003 Assessment of erosion of the ITER divertor targets during type I ELMs *Plasma Phys. Control. Fusion* **45** 1523
[16] Leonard A., Herrmann A., Itami K., Lingertat J., Loarte A., Osborne T., Suttrop W. and (The ITER Divertor Modeling, Database Expert Group and The ITER Divertor Physics Expert Group) 1999 The impact of ELMs on the ITER divertor *J. Nucl. Mater.* **266–9** 109–17
[17] Leonard A.W. 2014 Edge-localized-modes in tokamaks *Phys. Plasmas* **21** 090501
[18] Hutchinson I.H. *et al* 1994 First results from Alcator C-mod *Phys. Plasmas* **1** 1511–8
[19] Greenwald M. *et al* 2014 20 years of research on the Alcator C-mod tokamak *Phys. Plasmas* **21** 110501
[20] Golfinopoulos T. *et al* (Alcator C-mod team) 2014 External excitation of a short-wavelength fluctuation in the Alcator

C-mod edge plasma and its relationship to the quasi-coherent mode *Phys. Plasmas* **21** 056111
[21] Golfinopoulos T., LaBombard B., Burke W., Parker R.R., Parkin W. and Woskov P. 2014 Wide-frequency range, dynamic matching network and power system for fusion plasma antenna *Rev. Sci. Instrum.* **85** 043510
[22] Golfinopoulos T. 2014 The shoelace antenna: a device to induce short-wavelength fluctuations in the edge plasma of the Alcator C-mod tokamak *PhD Thesis* Massachusetts Institute of Technology (http://hdl.handle.net/1721.1/91031)
[23] LaBombard B. and Lyons L. 2007 Mirror Langmuir probe: a technique for real-time measurement of magnetized plasma conditions using a single Langmuir electrode *Rev. Sci. Instrum.* **78** 073501
[24] Hubbard A.E. *et al* (Alcator C-Mod Group) 2011 Edge energy transport barrier and turbulence in the I-mode regime on Alcator C-mod *Phys. Plasmas* **18** 056115
[25] Dominguez A. 2012 Study of density fluctuations and particle transport at the edge of I-mode plasmas *PhD Thesis* Massachusetts Institute of Technology (http://hdl.handle.net/1721.1/79261)
[26] Cziegler I. *et al* 2013 Fluctuating zonal flows in the I-mode regime in Alcator C-mod *Phys. Plasmas* **20** 055904
[27] Brunner D., Kuang A.Q., LaBombard B. and Burke W. 2017 Linear servomotor probe drive system with real-time self-adaptive position control for the Alcator C-mod tokamak *Rev. Sci. Instrum.* **88** 073501
[28] Tolias P. 2014 On secondary electron emission and its semi-empirical description *Plasma Phys. Control. Fusion* **56** 123002
[29] McCarthy W., LaBombard B., Brunner D. and Kuang A.Q. 2018 An assessment of methods to compute secondary electron emission yields for tungsten and molybdenum electrodes exposed to Alcator C-Mod boundary plasmas: impact on plasma potentials reported by Langmuir probes *Plasma Phys. Control. Fusion* **60** 035011
[30] Terry J., Maqueda R., Pitcher C., Zweben S., LaBombard B., Marmar E., Pigarov A. and Wurden G. 2001 Visible imaging of turbulence in the SOL of the Alcator C-mod tokamak *J. Nucl. Mater.* **290–3** 757–62
[31] Zweben S.J. *et al* 2002 Edge turbulence imaging in the Alcator C-mod tokamak *Phys. Plasmas* **9** 1981–9
[32] Lin Y. 2001 Experimental application and numerical study of reflectometry in the Alcator C-mod tokamak *PhD Thesis* Massachusetts Institute of Technology, PSFC Report RR-01-5 (http://hdl.handle.net/1721.1/8649)
[33] Stillerman J., Burke W. and LaBombard B. 2010 An optical timing verification system for Alcator C-mod *Fusion Eng. Des.* **85** 367–9
[34] LaBombard B. *et al* (Alcator C-Mod Team) 2011 Scaling of the power exhaust channel in Alcator C-mod *Phys. Plasmas* **18** 056104
[35] Xu X., Umansky M., Dudson B. and Snyder P. 2008 Boundary plasma turbulence simulations for tokamaks *Commun. Comput. Phys.* **4** 949–79
[36] Dudson B., Umansky M., Xu X., Snyder P. and Wilson H. 2009 BOUT++: a framework for parallel plasma fluid simulations *Comput. Phys. Commun.* **180** 1467–80
[37] Scott B.D. 2005 Drift wave versus interchange turbulence in tokamak geometry: linear versus nonlinear mode structure *Phys. Plasmas* **12** 062314
[38] Evans T.E. *et al* 2004 Suppression of large edge-localized modes in high-confinement DIII-D Plasmas with a stochastic magnetic boundary *Phys. Rev. Lett.* **92** 235003
[39] Jenkins T.G., Kruger S.E., Hegna C.C., Schnack D.D. and Sovinec C.R. 2010 Calculating electron cyclotron current drive stabilization of resistive tearing modes in a nonlinear magnetohydrodynamic model *Phys. Plasmas* **17** 012502
[40] Haye R.L., Isayama A. and Maraschek M. 2009 Prospects for stabilization of neoclassical tearing modes by electron cyclotron current drive in ITER *Nucl. Fusion* **49** 045005
[41] Kajiwara K., Sakamoto K., Oda Y., Hayashi K., Takahashi K. and Kasugai A. 2013 Full high-power modulation on a 170GHz 1MW ITER gyrotron with a triode magnetron injection gun *Nucl. Fusion* **53** 043013
[42] Mossessian D.A., Snyder P., Hubbard A., Hughes J.W., Greenwald M., LaBombard B., Snipes J.A., Wolfe S. and Wilson H. 2003 High-confinement-mode edge stability of Alcator C-mod plasmas *Phys. Plasmas* **10** 1720–6
[43] Goedbloed J., Holties H., Poedts S., Huymans G. and Kerner W. 1993 MHD spectroscopy: free boundary modes (ELMs) and external excitation of TAE modes *Plasma Phys. Control. Fusion* **35** B277–92
[44] Fasoli A. *et al* 1997 Alfvén eigenmode experiments in tokamaks and stellarators *Plasma Phys. Control. Fusion* **39** B287–301
[45] Carlstrom T., Burrell K., Groebner R., Leonard A., Osborne T. and Thomas D. 1999 Comparison of L-H transition measurements with physics models *Nucl. Fusion* **39** 1941
[46] Hutchinson I.H. 1992 One-dimensional full-wave analysis of reflectometry sensitivity and correlations *Plasma Phys. Control. Fusion* **34** 1225
[47] Naidu P.S. 1995 *Modern Spectrum Analysis of Time Series: Fast Algorithms and Error Control Techniques* (Boca Raton, FL: CRC Press)
[48] Brillinger D.R. 1975 *Time Series: Data Analysis and Theory* (*Int. Series in Decision Processes*) (New York: Holt, Rinehart & Winston of Canada Ltd)
[49] Oppenheim A.V. and Schafer R.W. 2009 *Discrete-Time Signal Processing* 3rd edn (Harlow: Prentice)
[50] Sears J. 2010 Measurement and interpretation of stable and unstable Alfvén Eigenmodes in the presence of fast ions in Alcator C-mod *PhD thesis* MIT (http://hdl.handle.net/1721.1/60179)
[51] Alves D., Coelho R., Klein A., Panis T. and Murari A. 2010 A real-time synchronous detector for the TAE antenna diagnostic at JET *IEEE Trans. Nucl. Sci.* **57** 577–82